energies

MDPI

Article

Auxiliary Heat System Design and Off-Design Performance Optimization of OTEC Radial Inflow Turbine

Yiming Wang [1,2,3], Yanjun Liu [1,2,3] and Qiang Zhang [1,2,3,*]

[1] School of Mechanical Engineering, Shandong University, Jinan 250061, China; wym798062625@163.com (Y.W.); lyj111@sdu.edu.cn (Y.L.)
[2] Key Laboratory of High-Efficiency and Clean Mechanical Manufacture, Shandong University, Jinan 250061, China
[3] National Demonstration Center for Experimental Mechanical Engineering Education, Shandong University, Jinan 250061, China
* Correspondence: zhangqiangd@163.com; Tel.: +86-139-5311-9560

Abstract: In this paper, solar energy is used as the auxiliary heat source of the ocean thermal energy radial inflow turbine, and the thermodynamic model of the circulation system is established. In addition, the ejector is introduced into the ocean thermal power generation system, and the process simulation is carried out using Aspen Plus V12. To address performance attenuation of the radial turbine under varying working conditions, shape optimization of a 30 kW OTEC radial turbine was conducted. Finally, the off-design performance variation in the radial inflow turbine is analyzed in the presence of a solar auxiliary heat source. The results show that the use of an auxiliary heat source can effectively improve the cycle efficiency of the system and is also conducive to the stable operation of the radial turbine. Under the condition of auxiliary heat source, the system cycle efficiency is increased by 2.269%.

Keywords: ocean thermal energy conversion; radial inflow turbine; multi-energy complementary; off-design performance analysis

Citation: Wang, Y.; Liu, Y.; Zhang, Q. Auxiliary Heat System Design and Off-Design Performance Optimization of OTEC Radial Inflow Turbine. *Energies* **2024**, *17*, 2767. https://doi.org/10.3390/en17112767

Academic Editors: Helena M. Ramos and Manolis Souliotis

Received: 12 April 2024
Revised: 31 May 2024
Accepted: 3 June 2024
Published: 5 June 2024

1. Introduction

The basic principle of ocean thermal energy conversion (OTEC) is to use the warm seawater on the surface of the ocean to heat certain low-boiling point materials and make them vaporize, or to make the seawater vaporize through pressure reduction in order to drive the turbine to generate electricity. The cold seawater from the deep sea is used to condense the spent vapor after the work is carried out, so that it becomes liquid again, forming a complete cycle [1]. In the past decade, the complementary power generation of solar and ocean thermal energy has primarily involved combining marine photovoltaic and ocean thermal power generation. However, due to the vastly different energy capturing methods, the photovoltaic and thermal power generation systems often operate independently in many complementary projects, failing to improve the overall efficiency. In contrast, ocean thermal resources and ocean thermal energy can better complement each other in generating electricity, and the overall efficiency of the system can be improved through the adoption of measures to produce by-products such as freshwater and hydrogen [2]. However, unlike land-based photovoltaic power generation, offshore photovoltaic equipment must withstand the effects of waves, wind, and seawater corrosion, posing challenges for practical engineering applications.

Due to the small temperature difference between cold and hot sources and small enthalpy drop between inlet and outlet of radial inflow turbine in the system, it is difficult to achieve high cycle power generation efficiency in the ocean thermal energy generation system [3,4]. To promote the practical application of ocean thermal energy power generation systems, increasing the solar auxiliary heat source was often employed to broaden the inlet

working condition range of radial inflow turbine and improve its work capacity, ultimately reducing the overall system's power generation cost.

Yamada N et al. proposed a solar-powered ocean thermal energy conversion (SOTEC) system and performed first-order performance simulations [5]. The results showed that the installation of solar collectors can effectively improve the thermal efficiency of the OTEC plant. Under daytime conditions, the net thermal efficiency of the SOTEC system operating with a 20 K temperature increase is 2.7 times higher than the efficiency of the OTEC system. Aydin H et al. designed a closed-cycle OTEC system with 100 kW of solar auxiliary heat and investigated the effect of two forms of auxiliary heat, namely, solar preheated seawater, and superheated mass, on the performance of the system [6]. The system using the R32 working medium has a power of 68 kW and a cycle efficiency of 71%. The simulation results show that the net power generation under both preheating and overheating conditions is 20–25% higher than the design point. Compared with solar preheating seawater, the working medium superheating method reduces the solar collector area and is a better way to improve the OTEC system. Dezhdar A et al. proposed a hybrid power generation system of solar energy and ocean temperature difference [7]. The paper studied the effects of solar radiation intensity, collector area and turbine inlet temperature on system performance. However, the system mainly uses the water temperature difference on the back of Karkheh dam to generate electricity, and both solar energy and ocean thermal energy are used as power sources for circulating pumps. There are four heat exchangers in the whole system, and the cycle efficiency is low. Tian Z et al. proposed an S-OTEC/AC system by adding a cold energy recovery module to the solar-assisted OTEC system. The inlet temperature, outlet pressure and flow rate of the turbine are studied. The results show that the flow rate is the key parameter affecting the performance of the system. The output power of the system is 89.32 kW. However, the solar auxiliary heat module is still separated from the OTEC system, and the heat from the solar collector is not directly transferred to the organic working medium that drives the turbine [8]. Bian Y N et al. proposed a kalina circulation system using ammonia working medium and solar energy auxiliary heat [9]. When the inlet pressure of the system exceeds 2.9 MPa, the energy saving effect is better than that of the stand-alone system. The shortcoming of these studies is that they only put forward the concept of using solar energy for auxiliary heating of OTEC system but did not consider the specific implementation of auxiliary heating, and the heat collection area of the solar collector used in the study is too large, which is unrealistic in the harsh marine environment.

The turbine is the core component of the OTEC system. The radial inflow turbine needs to operate efficiently in both design and off-design conditions. Therefore, it is particularly important to study the characteristics of radial inflow turbines under variable operating conditions [10,11]. Domestic and foreign scholars have conducted a large number of studies on the characteristics of radial inflow turbine operating conditions. Sauret E et al. [12,13] designed a 400 kW R143a working medium radial inflow turbine for geothermal power generation and used the Peng–Robinson equation in Ansys-CFX to conduct a numerical simulation of the radial inflow turbine. By adjusting the rotor speed, expansion ratio and different inlet temperature, the performance curve of the radial inflow turbine is obtained. The results indicated that increasing the rotor speed and flow rate improves turbine efficiency. Binder et al. [14] proposed a performance prediction method of radial inflow turbine under variable conditions based on flow, load and expansion ratio parameters, which was verified by experiments. In addition, a performance prediction method of the radial inflow turbine with an adjustable stator angle under clogged conditions was also studied. Kumar et al. [15] studied the performance of centripetal turbines under varying operating conditions by using the sensitivity analysis method. In his paper, an artificial neural network model was used to predict the efficiency range of centripetal turbines, and structural parameters with the greatest influence on performance were given based on the loss model. Kiyarash et al. [16] put forward an expansion machine optimization method that uses dynamic efficiency instead of constant efficiency. This method combined

with the DIRECT algorithm can quickly screen turbine size parameters under different working conditions. All these design and optimization methods are aimed at a single design condition, but they are not involved in the optimization methods of the radial inflow turbine with an auxiliary heat source.

In summary, radial inflow turbines have been applied in the field of thermal power generation for a long time, and the design and optimization of a radial inflow turbine under medium and high temperature working conditions are relatively mature. However, research on radial inflow turbines applied in the field of complementary power generation of ocean thermal energy and solar energy is still lacking. The widespread adoption of Ocean Thermal Energy Conversion systems has been hindered by factors such as the small operating temperature range and long cost payback period. In order to improve the application value of ocean thermal energy and reduce the power generation cost of OTEC system, in addition to increasing the temperature difference of cold and hot sources of OTEC system by introducing auxiliary heat sources, it is also necessary to optimize the radial turbine structure so that it can still run efficiently when the working condition changes.

2. Materials and Methods

2.1. Radial Inflow Turbine Auxiliary Heat System Design and Variable Operating Conditions Realization Methods

2.1.1. Mathematical Model of OTEC System without Auxiliary Heat

The Organic Rankine Cycle (ORC) is the most basic, controllable, and widely used form of circulation, generally including the radial inflow turbine, working medium pump, condenser, and evaporator as core components, along with auxiliary components such as collectors and preheaters. Figure 1 illustrates the ORC of the ocean thermal energy generation system. First, the working fluid is heated by the warm surface seawater into saturated steam, which flows into the radial inflow turbine. The steam expands, promoting the turbine rotor's rotation and power output. The spent steam from the turbine outlet passes through the collector and enters the condenser, where it is cooled and condensed into a liquid by the cold deep seawater. The liquid working fluid is then compressed by the working medium pump and flows into the evaporator, completing a system cycle.

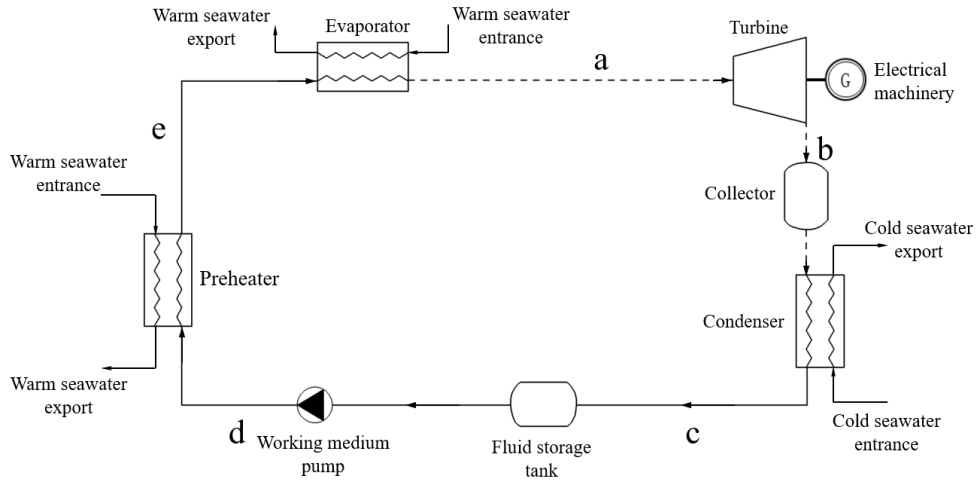

Figure 1. Rankine cycle ocean thermal energy conversion system. The letters a, b, c, d and e represent the thermodynamic state of the working medium at the evaporator outlet, turbine outlet, condenser outlet, pump outlet and preheater outlet, respectively.

The theoretical mathematical model of the cycle is as follows:

The preheater and evaporator are the isobaric heat absorption process ignoring heat loss; the preheater and evaporator energy conservation equation is

$$Q_w = m(h_a - h_d) = m_w c_w (T_{wi} - T_{wo}), \quad (1)$$

where is the Q_w evaporator heat absorption, h_e and h_d are the specific enthalpies of the evaporator outlet and inlet working medium, respectively, m is the mass flow rate of the working medium in the system, m_w is the mass flow rate of the surface seawater, c_w is the constant-pressure specific heat capacity of the surface seawater, T_{wi} and T_{wo} are the inlet and outlet temperatures of the surface seawater.

Inside the condenser is an isobaric and isothermal exothermic process, and the equation of conservation of energy is as follows:

$$Q_c = m(h_c - h_b) = m_c c_c (T_{ci} - T_{co}), \tag{2}$$

where Q_c is the heat dissipated by the condenser, h_c and h_b are the specific enthalpies of the condenser outlet and inlet masses, respectively, m_c is the mass flow rate of the cold seawater, c_c is the constant-pressure specific heat capacity of the cold seawater, and T_{ci} and T_{co} are the temperatures of the surface seawater inlet and outlet.

The thermodynamic process of the work material in the turbine is an isentropic expansion process, but the actual process is always accompanied by a certain increase in entropy, and its output power is as follows:

$$W_T = m(h_a - h_b)\eta_g \eta_s, \tag{3}$$

where h_a is the specific enthalpy of the inlet mass to the radial inflow turbine, η_g is the generator efficiency, and η_s is the entropy efficiency of the radial inflow turbine.

The thermodynamic process of the work material in the pump is an isentropic compression process, and the actual power consumption of the pump is as follows:

$$W_P = \frac{m(h_d - h_c)}{\eta_P}, \tag{4}$$

where η_P is the working medium pump efficiency.

The theoretical net output power of the ocean thermal energy generation system is

$$W_{net} = W'_T - W'_P, \tag{5}$$

where W'_T, W'_P is the power of the turbine and pump in the ideal case.

The cyclic theoretical efficiency is as follows:

$$\eta_{net} = \frac{W_{net}}{Q_w} = \frac{W'_T - W'_P}{m(h_a - h_d)} = \frac{(h_a - h_b) - (h_d - h_c)}{(h_a - h_d)}, \tag{6}$$

For the Organic Rankine Cycle without an auxiliary heat source, the ideal thermodynamic process temperature–entropy diagrams are shown in Figure 2, corresponding to the isentropic expansion process (1-2′), isothermal condensation process (2′-3), isentropic compression process (3-4), preheating process (4-5), and constant-pressure heat-absorption process (5-1), respectively. The actual thermodynamic process within the radial inflow turbine is (1-2-2′).

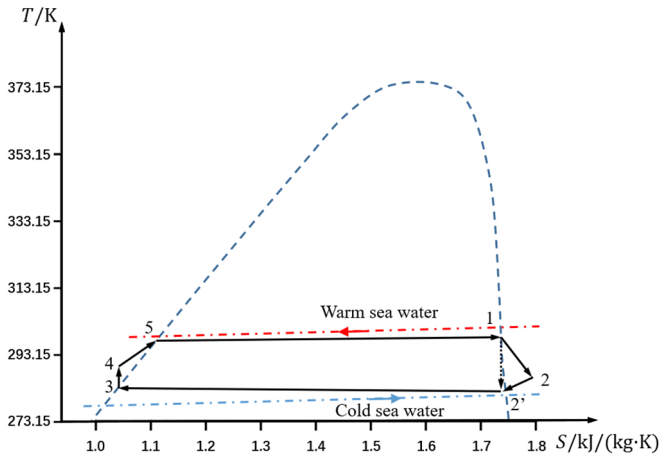

Figure 2. Organic Rankine Cycle temperature entropy diagram.

2.1.2. Design of Auxiliary Heat System

Due to the small temperature difference between the cold and heat sources in the Ocean Thermal Energy Conversion (OTEC) system, the theoretical cycle efficiency is low, hindering large-scale popularization and application. Introducing a solar energy auxiliary heat source is an effective solution to this problem. At present, OTEC plants with solar energy as an auxiliary heat source are primarily divided into two types: preheated seawater and superheated mass.

To substantially increase the temperature difference between the inlet and outlet of the OTEC radial inflow turbine and further reduce the effective area of the solar collector, this paper designs an OTEC system incorporating solar auxiliary heat based on the conventional Organic Rankine Cycle (ORC), as shown in Figure 3. Unlike the traditional ORC, in this system with auxiliary heat, the liquid working fluid pressurized by pump 1 is first heated by the preheater and then divided into two streams at point e. The diversion can be realized by adjusting the control parameters by two working medium pumps. After the diversion, about 80% of the working medium flows into the evaporator, which is heated by the surface warm seawater, and about 20% of the working medium is pressurized again by the working medium pump 2, and then sent to the solar collector for heating. The high-temperature, high-pressure gaseous working fluid from the solar collector outlet acts as the motivating fluid, transferring part of its kinetic energy and heat to the gaseous working fluid from the evaporator outlet. They are mixed within the ejector to form a medium-pressure gas that flows into the radial inflow turbine to perform work. In case of insufficient light intensity or at night, the stop valve 2 opens, the stop valve 1 and the working medium pump 2 shut down, and the system uses warm seawater as the only heat source for heating.

The work capacity of the radial inflow turbine depends mainly on the pressure at the inlet of the radial inflow turbine. Throughout the cycle, the phase change of the liquid working fluid is the process that absorbs the most external heat, while the pressurization of the gaseous working fluid after phase change absorbs little heat. Therefore, this paper introduces a solar collector and an ejector to separate the phase transformation process of most of the working fluid from the pressurization process. This portion of the working fluid is heated in an evaporator using warm seawater with a greater heat flow density to achieve a phase change, while the remaining working fluid undergoes phase transformation and pressurization in a solar collector. These streams are then mixed to obtain a medium-pressure gaseous working fluid, enhancing the work capacity of the radial inflow turbine.

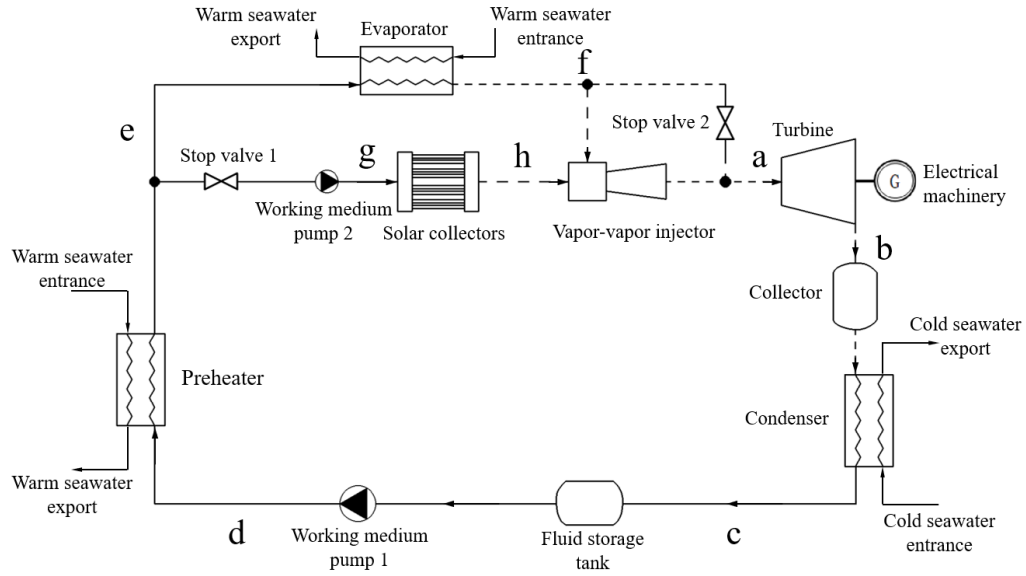

Figure 3. Rankine Cycle Ocean Thermal Energy Conversion system with solar-assisted heat. The letters a, b, c, d, e, f, g and h represent the thermodynamic state of the working medium at the turbine inlet, turbine outlet, condenser outlet, pump 1 outlet, preheater outlet, evaporator outlet, pump 2 outlet and solar collector outlet, respectively.

The theoretical mathematical model of the solar auxiliary heat branch is as follows:
The power consumption of the working medium pump 2 is

$$W_{P2} = \frac{m_2(h_g - h_e)}{\eta_P}, \tag{7}$$

where m_2 is the mass flow rate of the work mass flowing through the solar collector.
The amount of heat absorbed by the solar collector is

$$Q_{sw} = A_{sw} \cdot I \cdot \eta_{sw}, \tag{8}$$

where A_{sw} is the effective heat collection area of the solar collector, I is the solar radiation intensity, and η_{sw} is the thermal efficiency of the solar collector, and η_{sw} can generally take 0.55~0.65.
The theoretical heat absorption of the work mass flowing through the solar collector is

$$Q'_{sw} = m_2(h_h - h_g), \tag{9}$$

If the mass flow rate ratio of the solar auxiliary heat branch to the main circuit is set to be k,

$$k = \frac{m_2}{m}, \tag{10}$$

the theoretical efficiency of the cycle is as follows:

$$\eta_{net} = \frac{W'_T - W'_P - W'_{P2}}{Q_w + Q'_{sw}} = \frac{(h_a - h_b) - (h_d - h_c) - k(h_g - h_e)}{(h_a - h_d) - k(h_g - h_e)}, \tag{11}$$

where W'_{P2} is the power of the working medium pump 2 in the ideal case.
The system integrates the advantages of the OTEC system and solar power generation system. Compared to traditional solar power generation systems, it significantly reduces the effective heat collection area of the solar collector while maintaining higher system power generation. Although an additional working fluid pump increases the system's power consumption compared to traditional OTEC systems, the output power of the

radial inflow turbine increases simultaneously, while the heat absorbed from the external environment does not change significantly. It can be concluded from Formula (11) that the cycle efficiency of the system will be significantly improved.

The above ORC OTEC system with the introduction of solar auxiliary heat has two branches in the system with different thermodynamic processes of the work mass, and for the convenience of analysis, it is assumed that the cycling processes of the two work masses are independent of each other. For the working fluid flowing through the evaporator, the temperature and entropy change process is shown in Figure 4a. Unlike the ORC without auxiliary heat, part of the working fluid in the constant-pressure heat absorption process (5-1) becomes a gaseous working fluid that flows into the ejector. After energy transfer with the high-pressure working fluid from the solar collector outlet in the ejector, the temperature and entropy increase, forming a high-temperature superheated steam that flows into the radial inflow turbine to continue performing work. The actual thermodynamic process is (1-1′-2-2′). For the working fluid flowing through the solar collector, the temperature and entropy change process is shown in Figure 4b. Part of the working fluid undergoes the preheating process (4-5), corresponding to a second isentropic compression process (5-6) and constant-pressure heat absorption process (6-7-8). It then ejects the working fluid from the evaporator outlet in the ejector, resulting in an enthalpy drop (8-1′), and subsequently performs work by expanding in the radial inflow turbine. The actual process is (1′-2-2′).

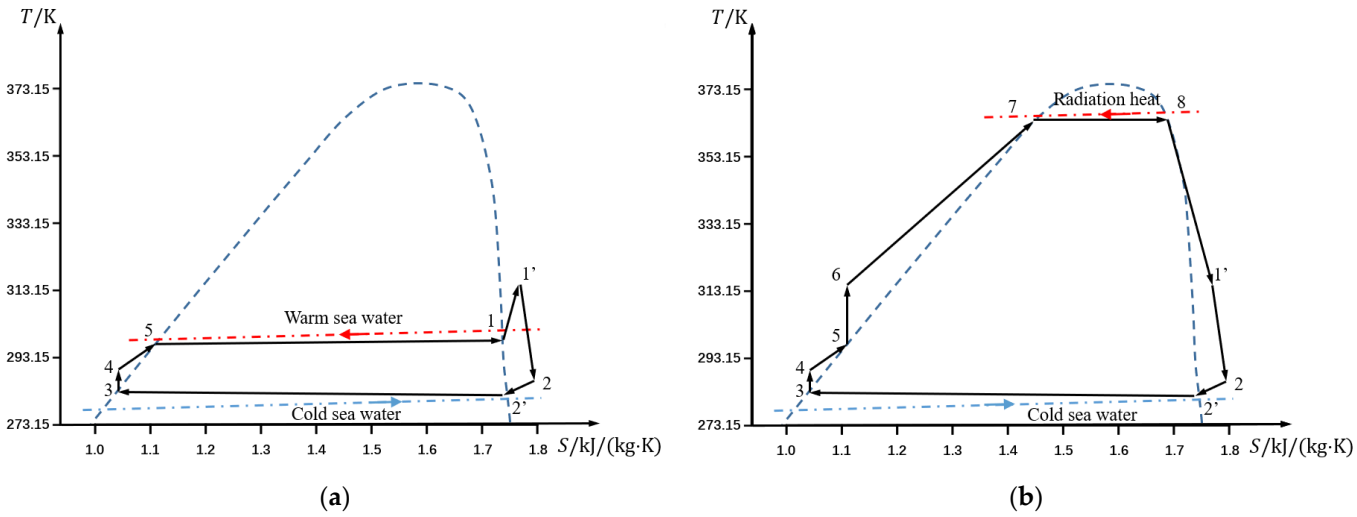

Figure 4. Working medium temperature entropy diagram of Rankine Cycle system with solar assisted heating. (**a**) Temperature entropy diagram of the working medium flowing through the evaporator; (**b**) temperature entropy diagram of the working medium flowing through a solar collector.

2.2. Process Simulation of Auxiliary Heat System

2.2.1. System Parameters Setting

The heat source temperature of the OTEC system was selected as 28 °C. Due to the limitation of deep-sea water temperature, the cold source temperature was selected as 4 °C, and the temperature difference between the inlet and outlet of the heat exchanger was set as 2 °C [17]. In this paper, the pipeline friction loss from the evaporator to radial inflow turbine is ignored, and R134a is selected as the circulating working medium, and the physical property parameters of R134a are obtained by invoking the working medium physical property database NIST REFPROP V9.1. In addition, after the working medium is heated by the solar collector, the temperature difference between the inlet and outlet of the radial inflow turbine is set as twice the traditional OTEC radial inflow turbine, and the inlet pressure is the saturation pressure of the corresponding temperature. The design parameters are shown in Table 1.

Table 1. OTEC system parameters comparison.

OTEC System Parameters (without Auxiliary Heat)	Values	OTEC System Parameters (with Auxiliary Heat)	Values
Total inlet pressure P_0/MPa	0.645	Total inlet pressure P_0/MPa	1.016
Total inlet temperature T_0/K	297.15	Total inlet temperature T_0/K	313.15
Outlet static pressure P_2/MPa	0.387	Outlet static pressure P_2/MPa	0.387
Mass flow rate m/(kg/s)	3.684	Mass flow rate m/(kg/s)	3.684
Isentropic efficiency η_s/%	≥85	Isentropic efficiency η_s/%	≥85
Rotating speed N/(r/min)	≤15,000	Rotating speed N/(r/min)	≤15,000
generated output P/kW	30	generated output P/kW	60

2.2.2. Circular Process Simulation by Aspen Plus

This paper establishes a graphical flow model based on Aspen Plus, sets parameters such as the operation type, phase state, and input/output conditions of different modules, and builds a cycle flow model of OTEC with solar auxiliary heat as shown in Figure 5. An ejector component was added to the system [18]. The system uses a mixer to simulate the ejector and uses the CFD simulation data of the ejector to correct the exit data of the mixer. The pressure distribution of the ejector in this paper is shown in Figure 6. In addition, in the experimental setup of the OTEC system, a warm water pump is typically used to transport warm water as the system's heat source. However, when the OTEC system is applied in the actual scenario, the warm sea water pump is a redundant component, and the power generation device can directly use the seawater heat exchanger to directly exchange heat with seawater [19]. The power consumption of the warm sea water pump is ignored in this simulation.

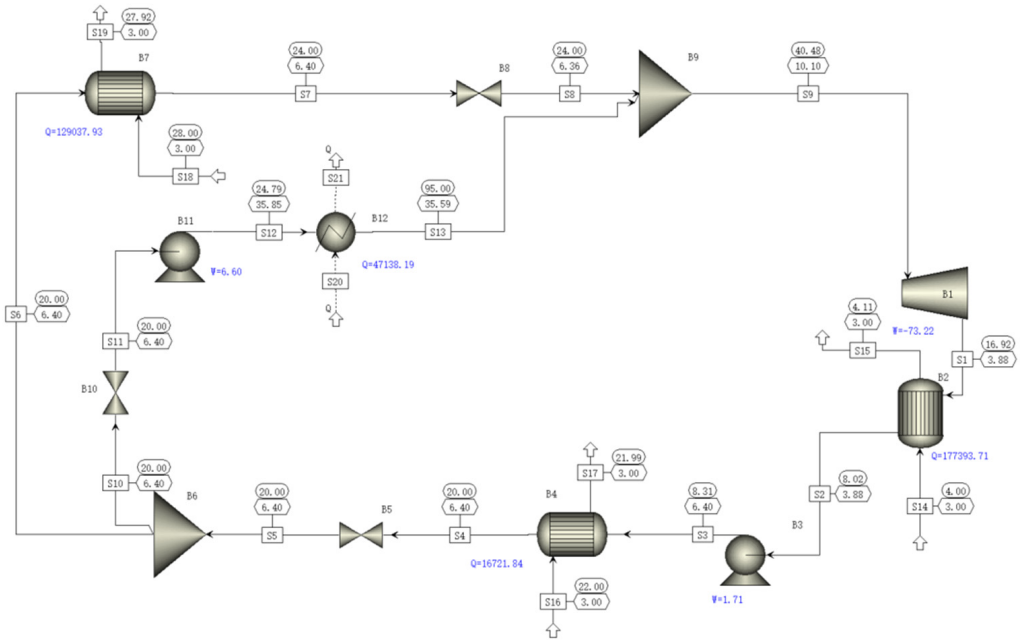

Figure 5. OTEC cycle process model with solar-assisted heating.

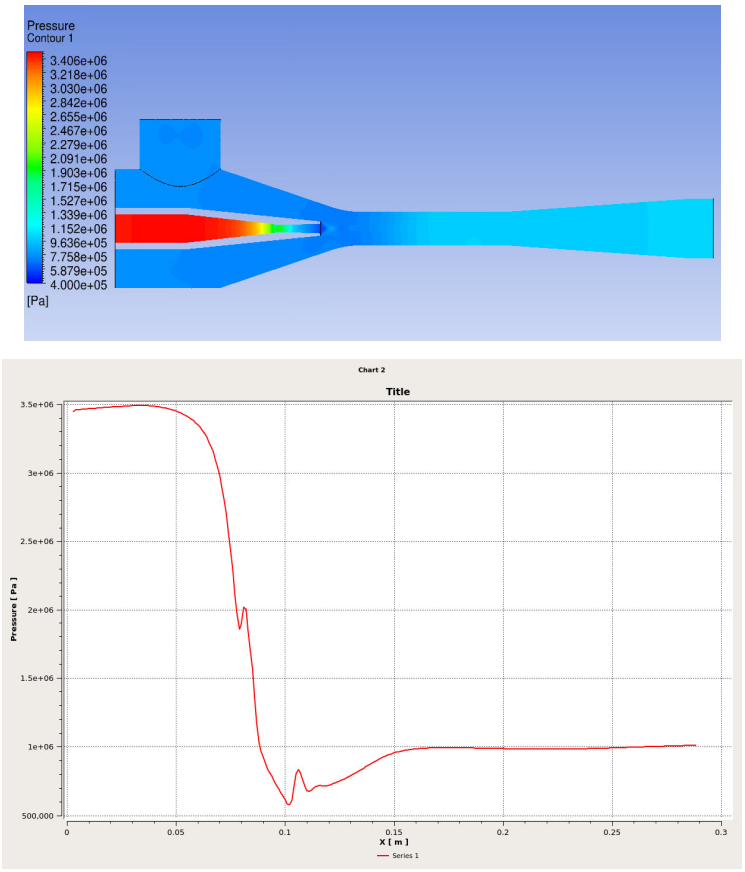

Figure 6. Pressure distribution diagram of cross section and pressure curve of central axis of ejector.

2.3. Optimization Method for the Performance under Off-Design Conditions of Radial Inflow Turbine

2.3.1. Modeling and Numerical Simulation of Radial Inflow Turbines

The off-design condition efficiency of the rotor is much lower than that of the volute and stator, so the optimized design of the radial inflow turbine rotor is the key point to improve the performance of the radial inflow turbine in the off-design condition [20]. In reference [21], rotor modeling was only optimized under conventional working conditions with an inlet total temperature of 297.15 K, and the rotor modeling was not necessarily applicable to other off-design working conditions under solar auxiliary heating conditions. In this paper, 40 groups of radial inflow turbine models in reference [21] were used, and the optimized radial inflow turbine scheme in reference [21] is taken as the initial scheme. The model simulation results under design conditions and its parameters are shown in Figure 7 and Table 2.

After using solar energy as an auxiliary heat source, the inlet temperature and pressure of the radial inflow turbine in the OTEC system changed from 297.15 K and 0.645 MPa to 313.15 K and 1.016 MPa, and the large fluctuation of the operating conditions would have a serious impact on the friction loss, internal leakage loss, and residual velocity loss of the radial inflow turbine.

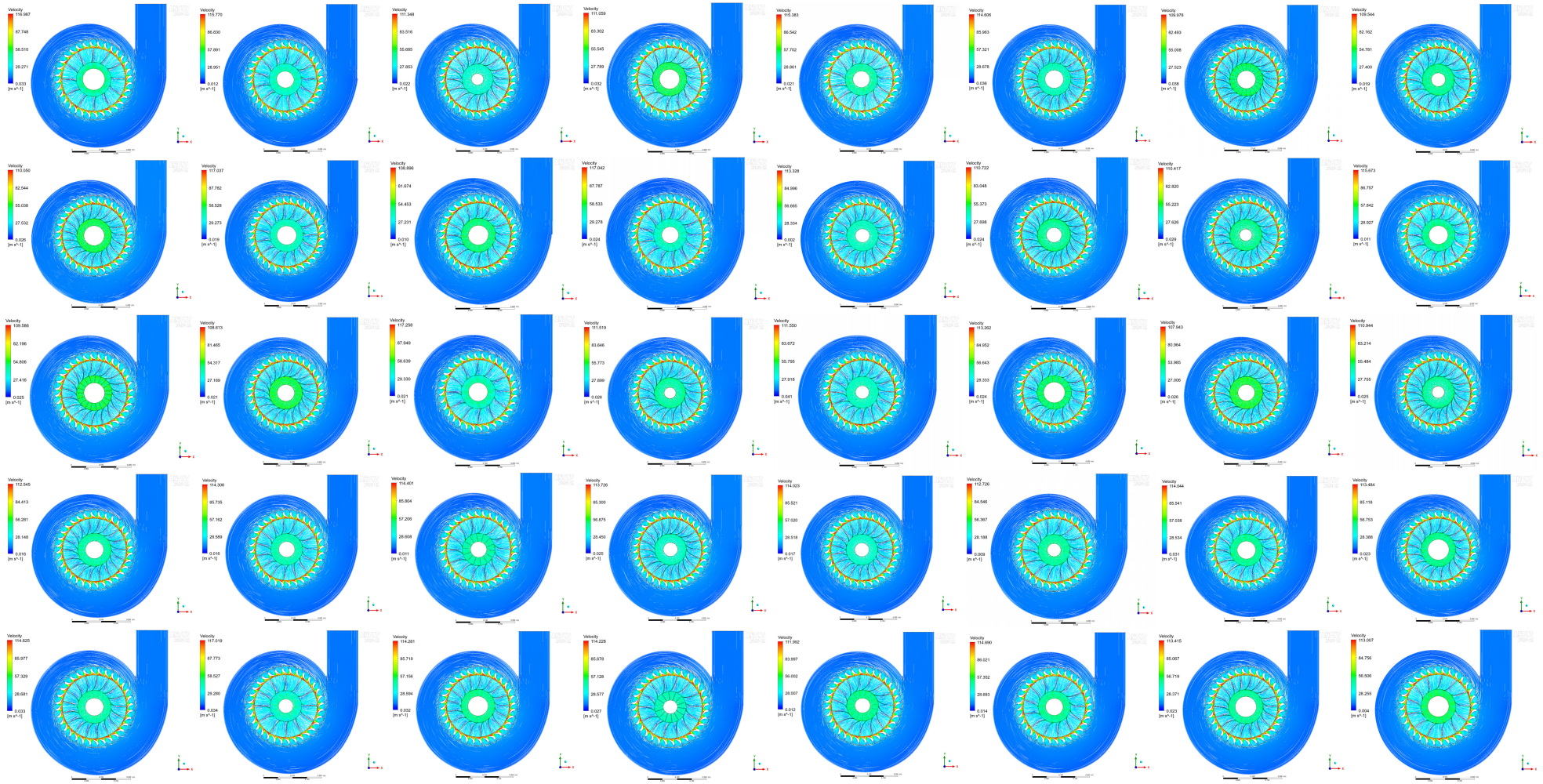

Figure 7. Model simulation results of 40 group radial inflow turbines.

Table 2. Initial model parameters of radial inflow turbine.

Parameters	Numerical Value	Parameters	Numerical Value
Reactivity Ω	0.479	Leaf gate inlet height l_N/mm	8.601
Aspect ratio $\overline{D}_2$	0.421	Impeller inlet diameter D_1/mm	217
Gear ratio $\overline{u}_1$	0.65	Outside diameter of rotor outlet $D_{2\prime}$/mm	110.83
Velocity coefficient of leaf grating φ	0.96	Inside diameter of rotor outlet $D_{2''}$/mm	52.78
Impeller speed coefficient ψ	0.85	Radial clearance Δ_1/mm	2.553
Absolute airflow angle at rotor inlet $\alpha_1/^\circ$	16.0	Leaf top clearance Δ_2/mm	0.273
Impeller outlet relative airflow angle $\beta_2/^\circ$	37.2	Blade thickness T_2/mm	1.582
Impeller inlet relative airflow angle $\beta_1/^\circ$	85.19	Blade outlet fillet radius r/mm	3.152
Impeller inlet circumferential speed u_1/(m/s)	93.17	Impeller blade twist angle $\theta/^\circ$	43.378
Impeller inlet absolute velocity c_1/(m/s)	99.32	Isentropic efficiency (physics) η_s/%	88.169
Impeller inlet relative speed ω_1/(m/s)	27.47	Shaft efficiency η_T/%	86.228
Absolute airflow angle at rotor outlet $\alpha_2/^\circ$	86.58	Number of revolutions per minute N/(r/min)	8200
Impeller outlet circumferential speed u_2/(m/s)	37.27	Number of leaf blades Z_1	32
Absolute velocity of rotor outlet c_2/(m/s)	29.46	Number of rotor blades Z_2	16
Impeller outlet relative velocity ω_2/(m/s)	48.86	Impeller axial length B_r	65.1

In order to study the performance of the initial scheme of the radial inflow turbine under variable operating conditions, this paper numerically simulates the initial scheme under four operating conditions. In addition, the shaft power P_T and shaft efficiency η_P are introduced as the evaluation criteria for the performance of the radial inflow turbine, which are defined by the following two equations.

$$P_T = \frac{T_r n}{9549} \tag{12}$$

$$\eta_P = \frac{P_T}{m h_s} = \frac{P_T}{m(i_0 - i_{2s})} \tag{13}$$

where T_r—Torque, N/m; n—Rotational speed, r/min; m—Mass flow rate, kg/s; h_s—Isentropic enthalpy drop per unit mass of working medium, kJ/kg; and i—Workmass enthalpy, kJ/kg, all given by CFD calculation.

The rotor optimization parameters of rotor are the wheel–diameter ratio $\overline{D}_2$, blade number Z_2, blade twist angle θ, radial clearance Δ_1, blade tip clearance Δ_2, blade outlet thickness T_2, and blade outlet fillet radius r. The sampling ranges and diagram for these parameters are shown in Table 3 and Figure 8.

Table 3. Sampling range of modeling parameters.

Parameters	Value
$\overline{D}_2$	0.38~0.468
Z_2	12~20
θ	35°~55°
Δ_1	2~3 mm
Δ_2	0.15~1.5 mm
T_2	1~3 mm
r	0.1~5 mm

The parameter $\overline{D}_2$ can be defined with the following formula.

$$\overline{D}_2 = \frac{\sqrt{D_{2\prime}^2 + D_{2''}^2}}{\sqrt{2} D_1} \tag{14}$$

The volute of initial scheme was modeled using SCDM and meshed using ICEM. The stator and rotor of the initial scheme were modeled using Bladegen and meshed using

Turbogrid. The grid numbers of the three flow channels are 700,229, 4,309,184 and 4,875,376, respectively. The grid details are shown in Figure 9.

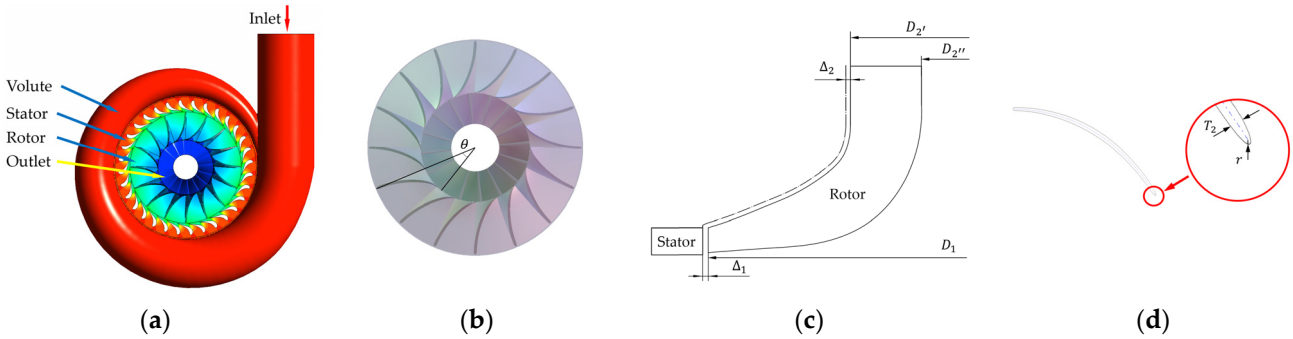

Figure 8. Impeller modeling parameters schematic diagram. (**a**) OTEC radial turbine appearance; (**b**) rotor blade twist angle θ at axial view; (**c**) radial clearance Δ_1 and tip clearance Δ_2 at meridian view; (**d**) rotor outlet blade thickness T_2 and rotor outlet blade fillet radius r at 50% leaf height cross section.

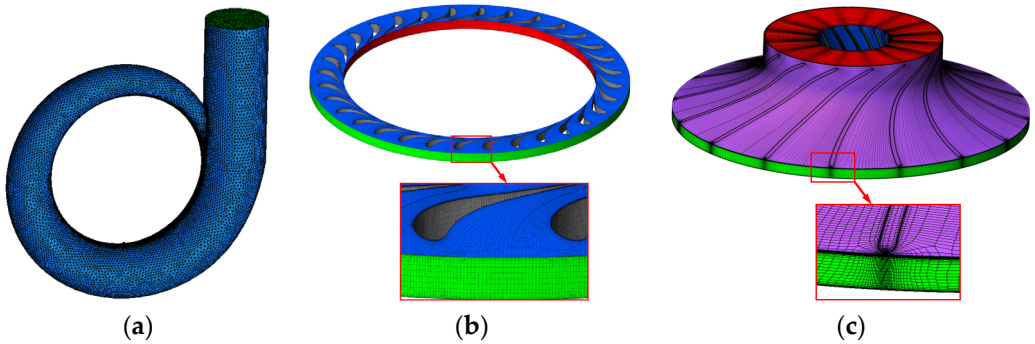

Figure 9. Mesh generation. (**a**) Volute mesh; (**b**) stator grid; (**c**) rotor mesh.

Figure 10 shows the result of grid independence verification. It can be seen that after the total number of grids exceeds 9 million, continuing to increase the number of grids has little impact on the simulation results, indicating that the set number of grids can meet the accuracy requirements. The meshing method of other schemes is consistent with the initial scheme.

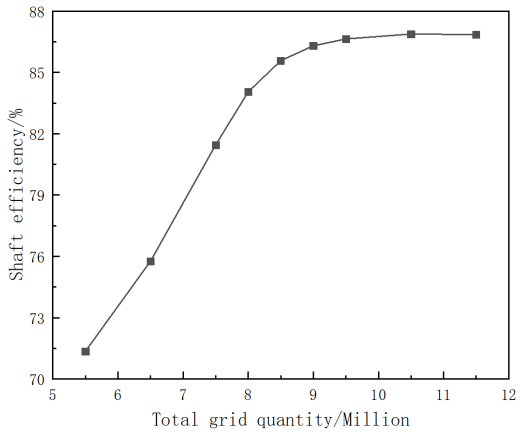

Figure 10. Grid independence verification.

Ansys-CFX was used for numerical simulation of these radial inflow turbines. The 40 groups of radial turbine models were, respectively, run under design conditions and three kinds of off-design conditions with solar auxiliary heat sources. The volute and stator, stator and rotor were set to statically connected and frozen rotor models, respectively, the

convergence residual was 10^{-6}, and all walls were set to no slip walls with roughness Ra3.2. When the OTEC radial inflow turbine is running under the design condition, the boundary conditions are set as the inlet total temperature of 297.15 K, the inlet total pressure of 0.645 MPa, and the outlet static pressure of 0.387 MPa. When operating under off-design conditions with auxiliary heat sources, the boundary conditions are set as inlet total temperature 303.15 K, 308.15 K and 313.15 K, the corresponding inlet total pressure is set as 0.765 MPa, 0.887 MPa and 1.016 MPa, and the outlet static pressure is consistent with the static pressure under design conditions.

2.3.2. Multi-Objective Optimization Method of Radial Inflow Turbine Based on Support Vector Regression and NSGA-III

By using the numerical simulation data in the previous section, a training sample library was established, and the support vector regression (SVR for short) prediction method was further adopted to establish the shaft efficiency prediction model of radial inflow turbines with different modeling parameters. The radial basis function was selected as the kernel function of the prediction model [20].

In order to find the rotor modeling parameters that will result in the highest efficiency of the radial inflow turbine shaft, this paper uses Non-dominated Sorting Genetic Algorithms III (NSGA-III for short) for multi-objective optimization of the rotor modeling parameters [22,23]. The design variables are the wheel diameter ratio $\overline{D}_2$, number of blades Z_2, blade torsion angle θ, radial clearance Δ_1, tip clearance Δ_2, blade exit thickness T_2 and blade exit fillet radius r.

Due to the introduction of a solar auxiliary heat source in this paper, the fluctuation range of inlet condition and impeller speed of radial inflow turbine has a large change. The performance of radial inflow turbine operating under an auxiliary heat condition is greatly different from that without an auxiliary heat condition, and the alternating load on the impeller is more complicated than that without auxiliary heat condition. Therefore, the performance, structural strength and operational reliability of the radial inflow turbine should be considered in the selection of impeller modeling parameters optimization objectives.

In this paper, optimization objectives of design condition shaft efficiency η_{P1}, off-design condition average efficiency η_{P2} and tip clearance Δ_2 are used to evaluate the performance of each radial inflow turbine scheme. Optimization objectives can be expressed as follows:

$$max\begin{Bmatrix} \eta_{P1}\left(\overline{D}_2, Z_2, \theta, \Delta_1, \Delta_2, T_2, r\right) \\ \eta_{P2}\left(\overline{D}_2, Z_2, \theta, \Delta_1, \Delta_2, T_2, r\right) \\ \Delta_2 \end{Bmatrix} \tag{15}$$

where η_{P1} is given directly by the prediction model, and η_{P2} is calculated by the following equation.

$$\eta_{P2} = 0.192\eta_{P30} + 0.206\eta_{P35} + 0.602\eta_{P40} \tag{16}$$

η_{P30}, η_{P35} and η_{P40} are the shaft efficiencies predicted value of radial inflow turbine at saturation conditions with inlet total temperature of 303.15 K, 308.15 K and 313.15 K. The coefficients 0.192, 0.206 and 0.602 are given according to the proportion of different solar radiation intensity to the whole day in Table 4. In addition, the purpose of making the tip clearance Δ_2 as large as possible is to avoid large friction losses.

Table 4. The proportion of different solar radiation intensities in the whole day.

Month	0~400 W/m^2	400~600 W/m^2	600~800 W/m^2	800~1000 W/m^2	1000~1200 W/m^2
1	65.19	6.05	8.47	17.07	3.23
2	64.51	8.05	7.05	9.77	10.63
3	65.73	8.47	6.45	8.6	10.75
4	65.69	8.05	4.72	8.48	13.05
5	63.84	7.8	7.66	8.87	11.83

Table 4. *Cont.*

Month	0~400 W/m^2	400~600 W/m^2	600~800 W/m^2	800~1000 W/m^2	1000~1200 W/m^2
6	65.27	8.75	13.06	8.33	4.59
7	65.05	9.94	9.95	10.75	4.3
8	66.4	7.93	10.48	9.14	6.05
9	67.5	9.17	8.89	7.64	6.8
10	72.44	9.94	9.81	5.77	2.02
11	71.26	7.92	8.61	10.56	1.67
12	72.59	8.47	8.88	10.08	0

3. Results

3.1. Auxiliary Heat System Process Simulation Results

The results of auxiliary heat system simulated by Aspen Plus are shown in Table 5.

Table 5. Cycle results of OTEC system with solar-assisted heating.

System Parameters (without Auxiliary Heat)	Results	System Parameters (with Auxiliary Heat)	Results
Power consumption of process pump 1/kW	1.508	Power consumption of process pump 1/kW	1.715
Power consumption of process pump 2/kW	0	Power consumption of process pump 2/kW	6.595
Turbine power/kW	33.16	Turbine power/kW	65.898
Evaporator heat absorption/kW	943.95	Evaporator heat absorption/kW	827.06
Collector Heat Absorption/kW	0	Collector Heat Absorption/kW	197.36
Net power generation/kW	31.652	Net power generation/kW	57.588
Cyclic efficiency/%	3.353	Cyclic efficiency/%	5.622

From the simulation results of Aspen Plus, it can be seen that the heat absorbed by the solar collector from the outside only accounts for 19.26% of the total heat absorption. The radial inflow turbine inlet pressure increases by 57.42% and the enthalpy drop increases by 88.28%, and the system cycle efficiency can reach 5.622% when the induced fluid is at 368.15 K. Compared to the ORC OTEC system without an auxiliary heat source, the cycle efficiency of this system is improved by about 2.27% from a base of 3.35%.

3.2. Numerical Simulation Results of 40 Groups of Radial Turbines

All the radial inflow turbine schemes are simulated under design conditions and saturation conditions with inlet total temperatures of 303.15 K, 308.15 K, and 313.15 K, respectively. The simulation results are post-processed in CFD-Post using the same method. Based on the torque T_r obtained from the simulation, we can obtain the 40 groups of radial inflow turbines under different operating conditions with the shaft efficiency, and the results are shown in Figure 11.

From the figure, it can be seen that the performance of the radial inflow turbine varies significantly with different design parameters for the rotor, and the statistics of the shaft efficiency data for the four operating conditions are shown in Table 6. From the data in the table, it can be seen that the simulation results of shaft efficiency in design condition have the smallest extreme deviation, the simulation results of shaft efficiency for the saturated condition at 303.15 K have the largest mean value, and the simulation results of shaft efficiency for the saturated condition at 308.15 K have the smallest degree of discretization. In addition, although the shaft efficiency values of each radial inflow turbine design scheme are different under four working conditions, the overall trend of shaft efficiency curves of radial inflow turbines under four working conditions is consistent. The design scheme

with excellent performance under the design condition generally has excellent performance under the other three conditions, which indicates that there may be a radial inflow turbine design scheme with excellent performance under multiple operating conditions.

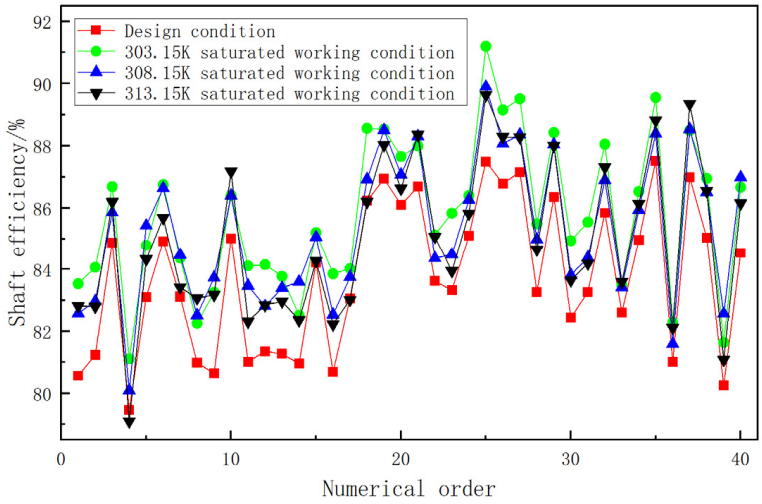

Figure 11. Efficiency distribution diagram of radial turbine shaft under different working conditions.

Table 6. Shaft efficiency data statistical results.

Working Condition	Extremely Poor	Average Value	Variance
Design condition	8.059	83.75	5.619
303.15 K saturated working condition	10.088	85.722	5.803
308.15 K saturated working condition	9.805	85.241	5.22
313.15 K saturated working condition	10.54	84.989	6.173

3.3. Comparison of Training and Prediction Results

Based on the 40 groups numerical simulation results of radial inflow turbine shaft efficiency, a training set is established, and then the nonlinear mapping relationship between rotor parameters and radial inflow turbine shaft efficiency can be obtained by using the SVR algorithm. By inputting different rotor parameters into the SVR model, the corresponding shaft efficiency prediction results can be obtained. In order to verify the prediction model, another 15 groups of radial inflow turbine models with different rotor parameters were established, and CFD simulation and SVR model prediction were carried out on them. The prediction results were taken as test set data to verify the accuracy of the SVR model. Under the design working conditions, 303.15 K, 308.15 K and 313.15 K saturation inlet conditions, the axial efficiency prediction results of the training set and the test set obtained by the SVR model were compared, as shown in Figure 12. The initial data of the training set are shown in Table 7.

As can be seen from the figure, there are some errors between the predicted results and the simulation results, but the errors of the test set and the training set are not large. The regression evaluation indexes are generally selected as the mean absolute error MAE, the root mean square error RMSE and the coefficient of determination R^2, and the calculation results of the three indexes are shown in Table 8.

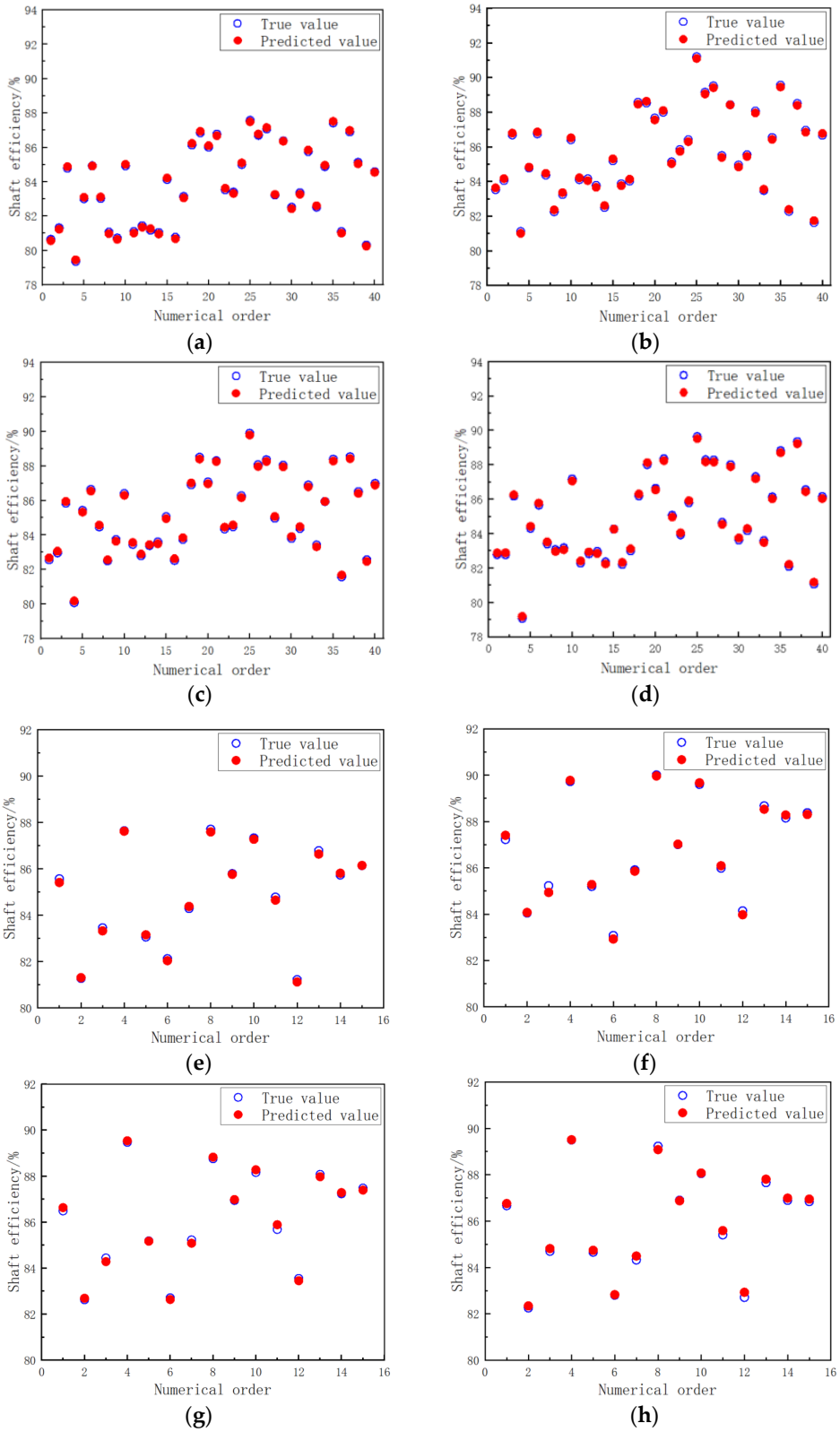

Figure 12. Prediction results comparison of turbine shaft efficiency under four rotor inlet working conditions. (**a**–**d**) Prediction results comparison of training set under design condition, 303.15 K saturated condition, 308.15 K saturated condition and 313.15 K saturated condition, respectively; (**e**–**h**) prediction results comparison of test set under design condition, 303.15 K saturated condition, 308.15 K saturated condition and 313.15 K saturated condition, respectively.

Table 7. Training set initial data.

Num.	$\bar{D}_2$	Z_2	θ	Δ_1	Δ_2	T_2	r	Design Condition	303.15 K Condition	308.15 K Condition	313.15 K Condition
1	0.468	12	37.56	2.44	1.08	2.23	2.74	80.648	83.533	82.575	82.807
2	0.423	13	38.59	2.95	1.14	1.51	0.73	81.315	84.065	82.971	82.791
3	0.382	16	45.77	2.77	0.85	1.00	3.12	84.799	86.688	85.854	86.197
4	0.448	15	51.92	2.41	1.36	2.74	1.61	79.374	81.108	80.090	79.094
5	0.418	13	44.23	2.36	0.92	2.85	5.00	83.018	84.788	85.429	84.330
6	0.439	18	36.54	2.46	0.79	1.41	4.87	84.926	86.753	86.642	85.678
7	0.441	20	53.97	2.64	1.01	1.36	3.74	83.037	84.371	84.476	83.421
8	0.396	16	52.44	2.23	1.40	1.97	3.87	81.063	82.259	82.513	83.067
9	0.457	19	45.26	2.67	1.04	2.80	4.25	80.723	83.254	83.734	83.176
10	0.445	15	37.05	2.15	0.66	1.31	0.60	84.934	86.412	86.401	87.173
11	0.448	16	39.62	2.77	0.82	2.90	0.48	81.097	84.113	83.468	82.311
12	0.414	13	40.64	2.18	1.27	1.15	3.24	81.436	84.151	82.808	82.845
13	0.400	17	36.03	2.74	1.33	2.33	3.37	81.183	83.770	83.400	82.961
14	0.407	19	48.33	2.90	1.20	2.03	0.85	81.041	82.506	83.597	82.354
15	0.385	18	42.69	2.38	0.69	3.00	1.11	84.140	85.202	85.059	84.270
16	0.443	14	47.31	2.92	1.24	1.67	4.50	80.763	83.856	82.535	82.226
17	0.452	19	49.36	2.21	0.72	2.13	0.35	83.139	84.027	83.749	83.016
18	0.427	19	51.41	2.85	0.28	2.49	2.24	86.148	88.565	86.921	86.204
19	0.434	12	42.18	2.56	0.31	1.26	3.49	86.853	88.533	88.504	88.031
20	0.380	17	54.49	2.33	0.56	1.77	1.23	86.020	87.654	87.071	86.625
21	0.389	16	41.67	2.05	0.40	1.87	3.87	86.767	87.998	88.308	88.355
22	0.464	15	49.87	2.08	0.88	1.72	4.12	83.536	85.130	84.362	85.068
23	0.421	18	53.46	2.10	0.63	2.95	3.62	83.400	85.833	84.489	83.945
24	0.387	20	46.28	2.62	0.76	2.18	4.62	85.017	86.401	86.269	85.817
25	0.432	18	47.82	2.31	0.18	1.05	2.49	87.573	91.196	89.895	89.633
26	0.416	15	40.13	3.00	0.34	2.39	4.37	86.704	89.151	88.074	88.291
27	0.412	14	46.79	2.82	0.24	1.92	0.23	87.078	89.511	88.362	88.281
28	0.403	20	43.21	2.13	1.11	1.21	1.98	83.234	85.489	84.984	84.646
29	0.405	19	35.51	2.69	0.47	1.62	1.48	86.372	88.424	88.046	88.005
30	0.391	14	50.38	2.87	0.98	2.64	2.36	82.509	84.942	83.814	83.649
31	0.436	14	52.95	2.51	0.95	1.10	0.98	83.354	85.541	84.388	84.191
32	0.466	17	43.72	2.97	0.53	1.46	2.11	85.762	88.055	86.897	87.310
33	0.430	17	38.08	2.00	1.14	2.54	2.61	82.524	83.486	83.420	83.593
34	0.398	12	35.00	2.49	0.60	2.44	1.86	84.881	86.533	85.945	86.134
35	0.455	17	39.10	2.28	0.21	2.54	2.99	87.435	89.552	88.394	88.818
36	0.394	14	44.74	2.26	1.30	2.08	0.10	81.093	82.281	81.586	82.110
37	0.409	15	55.00	2.59	0.37	1.82	4.75	86.910	88.495	88.535	89.344
38	0.425	13	48.85	2.03	0.50	2.28	1.36	85.122	86.950	86.514	86.554
39	0.461	18	41.15	2.54	1.43	1.56	1.73	80.303	81.637	82.566	81.082
40	0.459	13	50.38	2.72	0.44	2.69	2.86	84.580	86.670	86.988	86.153

Table 8. Regression evaluation index.

Regression Evaluation Indicators	Training Set Value	Test Set Value
MAE	0.0750	0.1116
RMSE	0.0773	0.1187
R^2	0.9989	0.9926

It can be seen from the relevant indicators in the table that the prediction results obtained by 40 groups of training samples are relatively reliable.

3.4. Multi-Objective Optimization of Radial Inflow Turbine Rotor Parameters Based on NSGA-III

The initial population of NSGA-III algorithm is set to 500, the number of evolutionary generations is set to 800, the crossover probability is set to 0.8, and the variance is set to 0.15. The Pareto front is obtained after calculation, as shown in Figure 13.

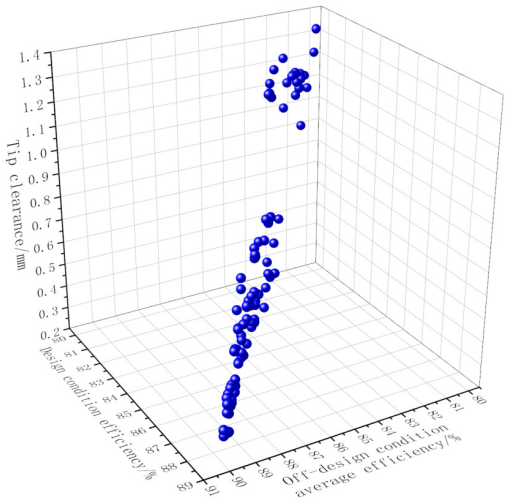

Figure 13. Pareto front distribution diagram.

As can be seen from the figure, most of the scatter points are distributed near the plane where the efficiency under design condition is equal to the average efficiency under off-design conditions. There is a significant trade-off between tip clearance and efficiency, with a higher density of high-efficiency scatter points for smaller tip clearances.

After screening the prediction results, schemes with η_{P1} less than 85% were removed, and the optimized scheme of rotor modeling parameters under variable working conditions was obtained, as shown in Table 9.

Table 9. Optimal modeling parameters based on optimization objective one.

Parameters	Initial Scheme	Scheme 1 (η_{P1max} and η_{P2max})	Scheme 2 (Δ_{2max})
$\overline{D}_2$	0.421	0.439	0.406
Z_2	16	17	16
$\theta/^\circ$	43.378	45.061	48.538
Δ_1/mm	2.553	2.532	2.507
Δ_2/mm	0.273	0.281	0.512
T_2/mm	1.582	1.666	1.987
r/mm	3.152	2.302	2.435
η_{P1}/%	88.467	87.993	85.705
η_{P2}/%	89.482	90.002	87.043

As can be seen from Table 9, Scheme 1 obtained by NSGA-III realizes both maximization of shaft efficiency under design conditions and maximization of average shaft efficiency under off-design conditions, while Scheme 2 realizes maximum tip clearance but experiences a significant performance decline in both design conditions and off-design working conditions.

4. Discussion

4.1. Comparative Analysis of Auxiliary Thermal Systems

Reference [5] proposes a cycle principle of a solar preheated seawater power generation scheme. The first-order modeling and simulation of solar-driven Ocean Thermal Energy Conversion system is carried out in the paper, and the results show that the annual average net thermal power of a 100 kW SOTEC plant can be up to 1.5 times of the conventional OTEC plant after the heat source temperature is increased by 20 K. However, to increase the heat source temperature by 20 K, the required effective area of single-glass flat-plate solar collector is at least 5000 m^2.

In this paper, the coupling power generation based on 60 kW OTEC system and solar energy is realized by reducing the working fluid flow of the auxiliary thermal branch and

increasing the ejector, and the inlet temperature of the radial inflow turbine is increased by 16 K. If the solar illumination intensity is between 600 W/m^2 and 1000 W/m^2, the solar collector power in Table 5 can be substituted into formula 8 to obtain the effective heat collection area of the solar collector, which is 303.63 m^2 to 598.06 m^2.

4.2. Performance Analysis of Variable Working Conditions

The introduction of a solar auxiliary heat source increases the inlet pressure of the radial inflow turbine, and the corresponding inlet temperature also needs to be increased simultaneously to ensure that the gaseous medium at the inlet has a certain degree of superheat, thus avoiding the generation of high-speed droplets on the rotor blades caused by liquid impact damage [24,25]. Therefore, when the inlet mass reaches a certain pressure, the corresponding saturation temperature is the lower limit value of the inlet temperature. The outlet pressure is set to 0.3876 MPa, and the rotor rotational speed is set to the theoretical rotational speed based on the isentropic enthalpy drop calculation. By numerical simulation of the optimized scheme 1 and scheme 2, the rotor torque of the radial inflow turbine under different saturation conditions can be obtained. Further calculation can obtain the curve of the radial inflow turbine output power and its shaft efficiency with respect to the inlet pressure, as shown in Figure 14.

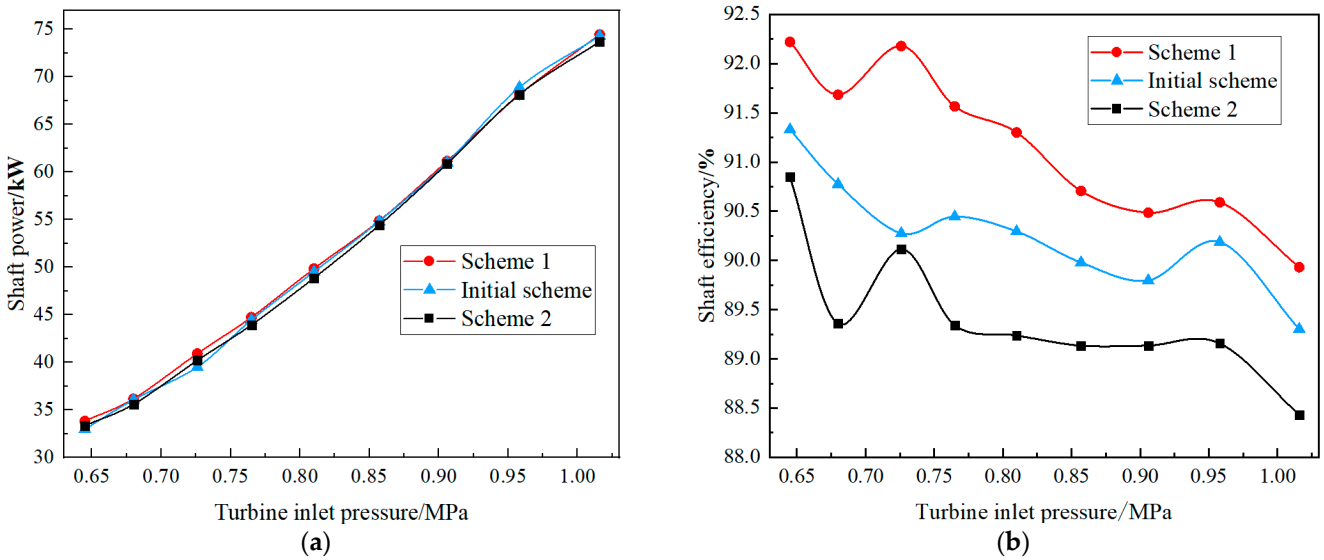

Figure 14. Curve of radial inflow turbine performance with inlet saturation pressure. (**a**) Curve of shaft power with inlet saturation pressure; (**b**) curve of shaft efficiency with inlet saturation pressure.

As can be seen from the figure, with the gradual increase in the inlet saturation pressure, the axial power of the radial inflow turbine increases, and the relationship between them is approximately linear. When the inlet pressure is 1.016 MPa, the axial power of every scheme reaches 74.45 kW, 74.28 kW and 73.7 kW, respectively. The shaft efficiencies fluctuate and decrease with the increase in inlet pressure. According to the performance curve of variable working conditions, after optimizing impeller modeling parameters with NSGA-III, the performance of scheme 1 is better than scheme 2 and initial scheme in the whole working range. Under the design condition of an inlet total pressure of 0.645 MPa and inlet total temperature of 297.15 K, the shaft efficiency reaches a maximum of 92.219%, while under the auxiliary heating condition of an inlet total pressure of 1.016 MPa and inlet total temperature of 313.15 K, the shaft efficiency reaches a minimum of 89.931%, a difference of 2.288%.

5. Conclusions

In this paper, based on the one-dimensional design of a 30 kW ocean thermal energy radial inflow turbine, the radial inflow turbine with a solar-assisted heat source has been optimized using three-dimensional numerical simulation, and the turbine's dynamic rotor modeling parameters have been optimized using multipurpose optimal methods, and the main conclusions obtained are as follows:

(1) Based on the ORC system, a solar collector and ejector were added, and the OTEC system with solar auxiliary heat was designed for the R134a working mass, and the mathematical model of the new OTEC system was established and process simulation calculations of the auxiliary heat working condition parameters were carried out. Finally, using Aspen Plus, the system cycle efficiency was calculated to be 2.269% higher than the cycle efficiency of the OTEC system without auxiliary heat.

(2) Under three different off-design conditions with auxiliary heat sources, 40 groups of radial turbines with different rotor modeling parameters were numerically simulated using CFX. Based on CFX-post 2020 R2 software, the simulation results of axial power and axial efficiency of these radial turbines were obtained through parameterization and batch processing. The simulation results of axial efficiency and axial power were used as training samples, and performance prediction models under different off-design conditions were established using the support vector regression method.

(3) The nonlinear mapping relationship between rotor modeling parameters and radial turbine shaft efficiency was obtained using the support vector regression prediction method. Further, the NSGA-III algorithm was used to optimize the radial inflow turbine's rotor parameters. The optimization objectives include design performance, off-design performance and tip clearance. The optimal scheme obtained by the multi-objective optimization algorithm also has the best performance under off-design condition. Under different off-design conditions, the optimal performance scheme, the initial scheme and the maximum tip clearance scheme were simulated by CFD, and the shaft power and shaft efficiency curves were obtained. The results show that with the increase in inlet pressure, the axial power tends to increase linearly, while the axial efficiency decline with fluctuation. The reason for the decrease in efficiency is that there is no auxiliary heat source in the initial design condition of all schemes, and the adaptability of impeller structure and working condition is the highest at low inlet pressure. The optimized scheme's performance is better than that of the original scheme over the entire off-design working range. The shaft efficiency under the design condition is 92.219%, which is 0.89% higher than the original scheme. Under the saturation condition of 313.15 K, the shaft efficiency is 89.93%, which is 0.628% higher than the initial scheme. In other off-design conditions, the shaft efficiency of the optimized scheme is also increased by 0.403–1.903%.

Author Contributions: Conceptualization, software, methodology, data curation, writing—original draft preparation and validation, Y.W.; conceptualization, supervision, and funding acquisition, Y.L. and Q.Z.; writing—review and editing, Q.Z.; project administration, Q.Z. All authors contributed to the design of the study. All authors discussed, read, edited, and approved the article. All authors have read and agreed to the published version of the manuscript.

Funding: This research was funded by the National Natural Science Foundation of China Basic Science Centre (Project No. 42188102) "Research on ocean carbon sinks and biological Geochemical Processes".

Data Availability Statement: The original contributions presented in the study are included in the article, further inquiries can be directed to the corresponding author.

Conflicts of Interest: The authors declare no conflicts of interest.

References

1. Chen, F.Y.; Liu, W.M.; Peng, J.P. Development and prospect of ocean thermal energy generation technology. *Green Sci. Technol.* **2012**, *11*, 246–248.

2. Park, S.; Chun, W.; Kim, N. Simulated production of electric power and desalination using solar-OTEC hybrid system. *Int. J. Energy Res.* **2017**, *41*, 637–649. [CrossRef]
3. Talluri, L.; Manfrida, G.; Ciappi, L. Exergo-economic assessment of OTEC power generation. *E3S Web Conf.* **2021**, *238*, 01015. [CrossRef]
4. Qixuan, C. Research on solar-assisted ocean thermal energy conversion system. *IOP Conf. Ser. Earth Environ. Sci.* **2021**, *687*, 012135–012137.
5. Yamada, N.; Hoshi, A.; Ikegami, Y. Performance simulation of solar-boosted ocean thermal energy conversion plant. *Renew. Energy* **2009**, *34*, 1752–1758. [CrossRef]
6. Aydin, H.; Lee, H.S.; Kim, H.J.; Shin, S.K.; Park, K. Off-design performance analysis of a closed-cycle ocean thermal energy conversion system with solar thermal preheating and superheating. *Renew. Energy* **2014**, *72*, 154–163. [CrossRef]
7. Dezhdar, A.; Assareh, E.; Keykhah, S.; Bedakhanian, A.; Lee, M. A transient model for clean electricity generation using solar energy and ocean thermal energy conversion (OTEC)-case study: Karkheh dam-southwest Iran. *Energy Nexus* **2023**, *9*, 100176. [CrossRef]
8. Tian, Z.; Zou, X.; Zhang, Y.; Gao, W.; Chen, W.; Peng, H. 4E analyses and multi-objective optimization for an innovative solar-ocean thermal energy conversion/air conditioning system. *J. Clean. Prod.* **2023**, *414*, 137532. [CrossRef]
9. Bian, Y.N.; Pan, J.X.; Liu, Y.; Zhang, F.; Yang, Y.; Arima, H. Performance analysis of a combined power and refrigeration cycle. *Energy Convers. Manag.* **2019**, *185*, 259–270. [CrossRef]
10. Schuster, S.; Markides, C.N.; White, A.J. Design and off-design optimisation of an Organic Rankine Cycle (ORC) system with an integrated radial turbine model. *Appl. Therm. Eng.* **2020**, *174*, 115192. [CrossRef]
11. Wu, T.; Shao, L.; Wei, X.; Ma, X.; Zhang, G. Design and structure optimization of small-scale radial inflow turbine for Organic Rankine Cycle system. *Energy Convers. Manag.* **2019**, *199*, 111940. [CrossRef]
12. Sauret, E.; Gu, Y.T. 3D CFD simulations of a candidate r143a radial-inflow turbine for geothermal power applications. In Proceedings of the ASME Power Conference 2014, Baltimore, MD, USA, 28–31 July 2014.
13. Sauret, E.; Gu, Y.T. Three-dimensional off-design numerical analysis of an Organic Rankine Cycle radial-inflow turbine. *Appl. Energy* **2014**, *135*, 202–211. [CrossRef]
14. Binder, N.; Carbonneau, X.; Chassaing, P. Off-design considerations through the properties of some pressure-ratio line of radial inflow turbines. *Int. J. Rotating Mach.* **2008**, *2008*, 273296. [CrossRef]
15. Kumar, M.; Panda, D.; Behera, S.K.; Sahoo, R.K. Experimental investigation and performance prediction of a cryogenic turboexpander using artificial intelligence techniques. *Appl. Therm. Eng.* **2019**, *162*, 114273. [CrossRef]
16. Rahbar, K.; Mahmoud, S.; Al-Dadah, R.K.; Moazami, N. Modelling and optimization of Organic Rankine Cycle based on a small-scale radial inflow turbine. *Energy Convers. Manag.* **2015**, *91*, 186–198. [CrossRef]
17. Chen, F.Y. Research on Thermal Performance and Comprehensive Utilization of Marine Thermal Energy Generation Device. Ph.D. Thesis, Harbin Engineering University, Harbin, China, 2016.
18. Wang, H.Y. Performance Simulation and Experimental Study of Ejector's Influence on Ocean Thermal Cycle. Master's Thesis, Shandong University, Jinan, China, 2020.
19. Wu, Z.J. Study on the Performance of Fork Row Tube Bundle Seawater Heat Exchanger under Sea Wave Conditions. Ph.D. Thesis, Tianjin University, Tianjin, China, 2020.
20. Yu, Z.T.; Wang, C.J.; Rong, F.H.; Liang, W. Optimal coupling design for Organic Rankine Cycle and radial turbine rotor using CFD modeling, machine learning and genetic algorithm. *Energy Convers. Manag.* **2023**, *275*, 116493.
21. Wang, Y.; Chen, Y.; Xue, G.; Zhang, T.; Liu, Y. Parameter optimization and performance research: Radial inflow turbine in ocean thermal energy conversion. *J. Mar. Sci. Eng.* **2023**, *11*, 2293. [CrossRef]
22. Deb, K.; Jain, H. An evolutionary many-objective optimization algorithm using reference-point-based nondominated sorting approach, part i: Solving problems with box constraints. *IEEE Trans. Evol. Comput.* **2014**, *18*, 577–601. [CrossRef]
23. Jain, H.; Deb, K. An evolutionary many-objective optimization algorithm using reference-point based nondominated sorting approach, part ii: Handling constraints and extending to an adaptive approach. *IEEE Trans. Evol. Comput.* **2014**, *18*, 602–622. [CrossRef]
24. Zhang, C.; Li, Y.; Tong, Z. Impact analysis and optimization of the preliminary design parameters for an Organic Rankine Cycle radial inflow turbine. *J. Braz. Soc. Mech. Sci. Eng.* **2023**, *45*, 10. [CrossRef]
25. Caballero, G.C.; Escorcia, Y.C.; Venturini, O.J.; Silva Lora, E.E.; Alviz Meza, A.; Mendoza Castellanos, L.S. Unidimensional and 3D analyses of a radial inflow turbine for an Organic Rankine Cycle under design and off-design conditions. *Energies* **2023**, *16*, 3383. [CrossRef]